

QUASARS PROBING QUASARS IX. THE KINEMATICS OF THE CIRCUMGALACTIC MEDIUM SURROUNDING $Z \sim 2$ QUASARS

MARIE WINGYEE LAU^{1,2}, J. XAVIER PROCHASKA², JOSEPH F. HENNAWI³

Draft version May 16, 2017

ABSTRACT

We examine the kinematics of the gas in the environments of galaxies hosting quasars at $z \sim 2$. We employ 112 projected quasar pairs to study the circumgalactic gas of the foreground quasars in absorption. The sample selects foreground quasars with precise redshift measurements, using emission-lines with precision $\lesssim 300 \text{ km s}^{-1}$ and average offsets from the systemic redshift $\lesssim |100 \text{ km s}^{-1}|$. We stack the background quasar spectra at the foreground quasar’s systemic redshift to study the mean absorption in C II, C IV, and Mg II. We find that the mean absorptions exhibit large velocity widths $\sigma_v > 300 \text{ km s}^{-1}$. The observed widths are consistent with gas in gravitational motion and Hubble flow, and galactic-scale outflows are not required to explain the large widths. Furthermore, we find that the mean absorptions are asymmetric about the systemic redshift. The mean absorption centroids exhibit small redshift relative to the systemic $\delta v \approx +200 \text{ km s}^{-1}$, with large intrinsic scatter in the centroid velocities of the individual absorption systems. We show that the observed offsets may be produced if (i) the ionizing radiation from the foreground quasars is anisotropic or intermittent; (ii) the gas is not flowing into the galaxy.

Keywords: galaxies: clusters: intracluster medium – galaxies: formation – galaxies: halos – intergalactic medium – quasars: absorption lines – quasars: general

1. INTRODUCTION

Galaxy formation and evolution are driven by the flows of gas into and out of their interstellar medium. Current theories demand that star-forming galaxies maintain these flows. Gas accretes, cools, and adds to the fuel supply, while star formation feedback heats gas, blows it out of galaxies, and regulates star formation (for a review see Somerville & Davé 2015).

Direct observations of galactic flows are difficult to acquire. Detecting the presence of the gas is itself challenging. Either the gas mass is too small, or the gas density is too low for the detection of line-emission, e.g. 21 cm, Ly α , or H α from H I. Resolving the kinematics and establishing the mass flux pose an even greater challenge. These challenges are accentuated for distant, young galaxies, where flows of gas are predicted to prevail (Kereš et al. 2009; Fumagalli et al. 2011). Therefore, with rare exceptions, (e.g. Cantalupo et al. 2014; Hennawi et al. 2015), the community has relied on absorption-line spectroscopy to detect and characterize the gas surrounding galaxies (e.g. Bergeron & Boisse 1991; Steidel et al. 2010; Prochaska et al. 2011; Tumlinson et al. 2013). In a previous paper of the Quasars Probing Quasars series (Lau et al. 2016, , hereafter QPQ8), we measured the velocity field for C II 1334 and C IV 1548, finding that the circumgalactic medium frequently exhibits large velocity widths that are offset from the systemic redshift. The offsets, δv , are often positive, with the sign convention that positive velocities indicate a redshift from the systemic. From a sample of 7 C II systems and 10 C IV

systems, we measured the velocity interval that encompasses 90% of the total optical depth, Δv_{90} , and the 1σ dispersion relative to the profile centroid, σ_v . The median Δv_{90} is 555 km s^{-1} for C II 1334 and is 342 km s^{-1} for C IV 1548. The median σ_v is 249 km s^{-1} for C II 1334 and is 495 km s^{-1} for C IV 1548. These velocity fields exceed all previous measurements from galaxies and/or absorption systems at any epoch.

With absorption-line spectroscopy of background sightlines, other researchers also have had success in characterizing the flows of gas around galaxies. Rakic et al. (2012) found a net large-scale inflow around star-forming galaxies, or a Kaiser effect for gas on 1–2 Mpc scales. Johnson et al. (2015) studied the CGM surrounding $z \sim 1$ quasars, and found large peculiar motions in the gas exceeding the expected virial velocity, which they interpret as quasar-driven outflows. However, the velocity spreads were not well quantified. Other existing studies that found large velocity spreads are limited to single sightlines with most of the gas within several hundred km s^{-1} (e.g., Tripp et al. 2011), or with gas tracing a higher ionization state than the QPQ absorption systems (e.g., Churchill et al. 2012), or where the average velocity spread is smaller than that measured in QPQ8 (e.g., Gauthier 2013; Muzahid et al. 2015; Zahedy et al. 2016).

A significant limitation of absorption-line analysis of transverse sightlines, especially regarding galactic-scale flows, is the inherent symmetry of the experiment. One generally lacks any constraint on the distance of the gas along the sightline. Positive or negative velocities with respect to the galaxy may be interpreted as gas flowing either toward or away from the system. “Down-the-barrel” observations break this symmetry, and have generally provided evidence for flows away from galaxies (Rupke et al. 2005; Martin 2005; Weiner et al. 2009; Rubin et al. 2014). However, these data are frequently at

¹ Email: lwymarie@ucolick.org

² Department of Astronomy and Astrophysics, UCO/Lick Observatory, University of California, 1156 High Street, Santa Cruz, CA 95064

³ Department of Physics, Broida Hall, University of California, Santa Barbara, CA 93106-9530

low spectral resolution which limits one’s sensitivity to inflowing gas.

In this paper (hereafter QPQ9), we examine the flows of gas in the environments of massive galaxies hosting quasars. Our approach leverages a large dataset of quasar pairs (Hennawi et al. 2006, , hereafter QPQ1) to use the standard techniques of absorption-line spectroscopy with background quasars. These quasar pairs have angular separations that correspond to less than 300 kpc projected separation at the foreground quasar’s redshift. Our previous publications from these quasar pairs have established that these galaxies are surrounded by a massive, cool, and enriched CGM (QPQ5, QPQ6, QPQ7: Prochaska et al. 2013b,a, 2014). We have collected a sample of 112 background spectra that are paired with foreground quasars with precisely measured redshifts. Among the sightlines in the QPQ9 sample, 13 have spectral resolution $R > 5000$ from echellette or echelle observations, and have been analyzed separately in QPQ8. Our primary scientific interests are twofold: (i) search for signatures of galactic-scale outflows from the central galaxy, presumably driven by recent star forma-

tion and/or active galactic nuclei feedback; (ii) characterize the dynamics of the gas around these massive systems. We further describe an aspect of this experiment that offers a unique opportunity to study galactic-scale flows: we argue that, the anisotropic or intermittent radiation from the foreground quasars may break the symmetry in the velocity field of circumgalactic absorbers. If the ionizing radiation field is asymmetric, the absorbers may also distribute asymmetrically. Alternatively, finite quasar lifetime will result in different radiation fields impinged on the gas closer to versus further away from the background quasar, due to different light travel times. Kirkman & Tytler (2008) reported an asymmetry in H I absorption on scales larger than the CGM, and gave similar arguments on anisotropy or intermittence.

We adopt a Λ CDM cosmology with $\Omega_M = 0.26$, $\Omega_\Lambda = 0.74$, and $H_0 = 70 \text{ km s}^{-1} \text{ Mpc}^{-1}$. Distances are proper unless otherwise stated. When referring to comoving distances we include explicitly an h^{-1} term and follow modern convention of scaling to a Hubble constant of $70 \text{ km s}^{-1} \text{ Mpc}^{-1}$.

2. THE EXPERIMENT

Table 1
Properties of the Projected Quasar Pairs in the QPQ9 sample

Foreground Quasar	z_{fg}	Line for z_{fg}^a	Background Quasar	z_{bg}	BG Quasar Instrument	R_\perp (kpc)	g_{UV}
J004238.24+135054.8	1.7766	SDSS-HW	J004236.53+135037.3	1.894	BOSS	266	386
J004757.26+144741.0	1.6202	SDSS-HW	J004757.88+144744.7	2.757	BOSS	82	6705
J005717.36-000113.3	2.1606	[OIII]	J005718.99-000134.7	2.511	BOSS	271	1283
J010323.84-000254.2	1.7543	SDSS-HW	J010324.37-000251.3	2.306	BOSS	74	5488
J014917.11-002141.6	1.6834	MgII	J014917.46-002158.5	2.159	SDSS	155	2390
J021416.96-005229.1	1.8025	SDSS-HW	J021416.12-005251.5	2.332	BOSS	225	566
J022447.89-004700.4	1.6964	SDSS-HW	J022448.85-004638.9	2.188	BOSS	226	294
J023018.27-033319.4	2.3817	MgII	J023019.99-033315.0	2.985	BOSS	221	1444
J023946.43-010640.4	2.2985	[OIII]	J023946.45-010644.1	3.124	BOSS	32	20931
J025038.69-004739.1	1.8529	SDSS-HW	J025039.82-004749.6	2.444	BOSS	174	4033
J034138.16+000002.9	2.1246	MgII	J034139.19-000012.7	2.243	GMOS-N	190	392
J040955.87-041126.9	1.7166	MgII	J040954.21-041137.1	2.0	MagE	235	715
J075259.81+401128.2	1.8844	MgII	J075259.14+401118.2	2.121	SDSS	110	1060
J080049.89+354249.6	1.982	[OIII]	J080048.74+354231.3	2.066	LRIS	201	2074
J080945.17+453918.1	2.0418	SDSS-HW	J080948.22+453929.0	2.278	BOSS	292	195
J081223.17+262000.9	1.6436	SDSS-HW	J081223.89+262012.5	2.17	BOSS	132	3446
J081832.87+123219.9	1.702	SDSS-HW	J081833.97+123215.4	2.234	BOSS	147	6606
J082642.86+470829.5	1.7992	SDSS-HW	J082644.64+470803.9	1.861	SDSS	274	250
J082843.37+454517.3	1.873	MgII	J082844.87+454518.2	1.987	LRIS	137	525
J083030.38+545228.8	1.6724	SDSS-HW	J083029.11+545210.3	3.337	BOSS	188	1509
J083713.56+363037.3	1.8364	MgII	J083712.69+363037.7	2.301	MODS1	92	5012
J083757.91+383727.1	2.0624	H α	J083757.13+383722.4	2.251	LRIS	89	8609
J083854.52+462124.4	1.7614	SDSS-HW	J083852.94+462137.6	2.163	BOSS	184	675
J084158.47+392120.0	2.0409	[OIII]	J084159.26+392139.0	2.214	LRIS	183	1514
J085358.36-001108.0	2.4011	[OIII]	J085357.49-001106.2	2.579	MagE	112	1231
J085629.48+551450.2	1.6218	SDSS-HW	J085630.45+551417.5	1.932	BOSS	296	466
J085737.58+390120.5	1.954	SDSS-HW	J085738.00+390136.0	2.848	BOSS	150	1987
J090250.02+360255.1	1.7613	SDSS-HW	J090247.78+360234.6	2.305	BOSS	298	238
J090417.94+004148.2	1.6185	SDSS-HW	J090419.12+004205.1	1.645	SDSS	214	1034
J090657.78+100121.4	1.698	SDSS-HW	J090657.62+100105.6	2.525	BOSS	141	6972
J091046.44+041458.5	2.0456	[OIII]	J091046.69+041448.4	2.377	MagE	95	11897
J091217.57+413933.5	1.7775	SDSS-HW	J091215.75+413948.2	2.198	BOSS	220	792
J091234.27+305616.2	1.6224	SDSS-HW	J091236.32+305626.5	2.146	BOSS	247	514
J091338.33-010708.7	2.7491	MgII	J091338.97-010704.6	2.916	XSHOOTER	89	5830
J091432.02+010912.4	2.1399	[OIII]	J091430.85+010927.5	2.475	BOSS	199	1222
J091551.72+011900.2	1.9719	SDSS-HW	J091553.37+011911.4	2.102	BOSS	236	972
J092417.65+392920.3	1.8864	MgII	J092416.72+392914.6	2.08	LRIS	106	2788
J093226.34+092526.1	2.4167	[OIII]	J093225.66+092500.2	2.602	MagE	238	774
J093317.43+592027.4	1.8588	SDSS-HW	J093320.57+592036.5	2.633	BOSS	224	1437
J093530.89+453226.9	2.093	SDSS-HW	J093530.78+453256.4	3.417	BOSS	254	537
J093640.35-005840.1	2.2098	MgII	J093642.12-005831.3	2.731	BOSS	250	496
J094133.64+230840.1	1.7735	SDSS-HW	J094135.61+230845.8	2.551	BOSS	243	1696
J100046.45+033708.8	1.6997	SDSS-HW	J100048.52+033708.8	2.353	BOSS	271	255
J100509.56+501929.8	1.8176	MgII	J100507.07+501929.8	2.019	LRIS	211	330
J100627.47+480420.0	2.3029	[OIII]	J100627.11+480429.9	2.597	BOSS	90	2886

Table 1 — *Continued*

Foreground Quasar	z_{fg}	Line for z_{fg}^a	Background Quasar	z_{bg}	BG Quasar Instrument	R_{\perp} (kpc)	g_{UV}
J100913.91+023612.4	1.7365	SDSS-HW	J100913.33+023643.0	2.216	BOSS	287	342
J100941.35+250104.1	1.8703	MgII	J100940.58+250053.9	1.981	LRIS	127	3588
J101001.51+403755.5	2.1924	H α	J101003.47+403754.9	2.505	BOSS	191	5421
J101323.89+033016.0	1.9428	SDSS-HW	J101322.23+033009.1	2.273	BOSS	219	428
J101753.38+622653.4	1.6535	SDSS-HW	J101750.44+622648.2	2.738	BOSS	184	923
J102007.23+611955.0	1.7887	SDSS-HW	J102010.05+611950.3	2.387	BOSS	180	1813
J102443.99+261615.1	1.8941	SDSS-HW	J102443.17+261602.7	2.158	BOSS	144	1960
J103443.62+085702.0	1.6379	SDSS-HW	J103442.26+085645.7	2.766	BOSS	233	699
J103628.12+501157.9	2.0033	SDSS-HW	J103630.52+501219.8	2.228	BOSS	271	1191
J103857.37+502707.0	3.1319	[OIII]	J103900.01+502652.8	3.236	ESI	233	3567
J104244.84+650002.7	1.987	SDSS-HW	J104245.14+645936.7	2.124	BOSS	227	703
J104435.62+313950.7	1.7071	SDSS-HW	J104434.76+313957.7	2.377	BOSS	115	1875
J105221.77+555253.5	1.9956	SDSS-HW	J105218.36+555311.3	2.278	BOSS	293	844
J110617.17+463524.6	1.6026	SDSS-HW	J110617.02+463520.4	2.732	BOSS	40	15381
J111339.86+330604.8	1.8929	SDSS-HW	J111337.84+330553.3	2.413	BOSS	243	855
J111850.44+402553.8	1.9238	SDSS-HW	J111851.45+402557.6	2.317	BOSS	106	1944
J113852.65+632934.0	1.8849	SDSS-HW	J113851.73+632955.6	2.625	BOSS	196	1912
J114435.54+095921.7	2.9727	[OIII]	J114436.65+095904.9	3.16	MIKE-Red	189	2914
J114546.54+032236.7	1.7664	MgII	J114546.22+032251.9	2.011	MagE	139	779
J115253.09+150706.5	1.7931	SDSS-HW	J115254.97+150707.8	3.349	BOSS	237	626
J115533.62+393359.2	1.612	SDSS-HW	J115531.32+393415.4	2.555	BOSS	272	742
J120224.68+074800.3	1.6622	SDSS-HW	J120226.48+074739.7	2.767	BOSS	296	584
J120417.47+022104.7	2.4355	[OIII]	J120416.69+022110.0	2.532	HIRES	112	2710
J120856.94+073741.2	2.1708	MgII	J120857.16+073727.3	2.616	MagE	123	3853
J121159.88+324009.0	1.9813	SDSS-HW	J121201.69+324013.3	2.273	BOSS	209	1050
J121344.28+471958.7	1.8325	SDSS-HW	J121343.01+471931.0	3.275	BOSS	260	488
J1215590+571616.6	1.9295	[OIII]	J121558.82+571555.5	1.964	SDSS	184	614
J122514.29+570942.3	1.8977	SDSS-HW	J122517.89+570943.7	2.224	BOSS	255	331
J123143.01+002846.3	3.2008	[OIII]	J123141.73+002913.9	3.308	GMOS-S	271	1490
J124002.23+395555.5	1.8422	SDSS-HW	J123959.88+395544.3	2.556	BOSS	256	245
J124420.84+391607.0	1.9979	SDSS-HW	J124419.52+391613.5	2.351	BOSS	141	927
J124431.37+320823.9	1.9916	SDSS-HW	J124432.96+320826.4	2.188	BOSS	176	669
J124632.33+234531.2	1.9949	SDSS-HW	J124632.19+234509.5	2.573	BOSS	188	1889
J124846.05+405758.2	1.8259	SDSS-HW	J124846.97+405820.9	2.463	BOSS	219	897
J130124.74+475909.6	2.194	H α	J130125.67+475930.8	2.765	SDSS	159	4932
J130605.19+615823.7	2.1089	H α	J130603.55+615835.2	2.175	LRIS	141	1761
J132514.97+540930.6	2.0469	SDSS-HW	J132511.07+540927.0	3.235	BOSS	298	513
J134650.08+195235.2	2.0681	SDSS-HW	J134648.19+195253.1	2.523	BOSS	278	883
J135632.42+613300.6	2.024	SDSS-HW	J135629.54+613310.2	2.17	LRIS	197	485
J135849.71+273806.9	1.9008	MgII	J135849.54+273756.9	2.127	LRIS	89	1765
J141337.18+271517.1	1.6905	MgII	J141337.96+271511.0	1.965	BOSS	105	609
J142003.67+022726.7	3.6162	[OIII]	J142004.12+022708.8	4.191	ESI	144	2291
J142054.42+160333.3	2.0216	[OIII]	J142054.92+160342.9	2.057	MagE	104	7811
J142215.57+465230.7	1.7475	SDSS-HW	J142214.63+465254.6	2.338	BOSS	225	639
J142758.89-012130.4	2.2733	[OIII]	J142758.74-012136.2	2.354	MIKE	53	34208
J143109.67+572728.0	1.6802	MgII	J143109.22+572726.4	2.063	BOSS	39	5166
J143312.56+082651.8	1.8812	SDSS-HW	J143313.99+082714.0	2.432	BOSS	274	531
J143345.55+064109.0	2.2934	[OIII]	J143344.55+064111.9	2.34	BOSS	122	1130
J144232.92+013730.4	1.8079	MgII	J144231.91+013734.8	2.274	BOSS	137	1988
J150814.06+363529.4	1.8493	MgII	J150812.78+363530.3	2.105	BOSS	133	5111
J153328.83+142542.5	2.0782	MgII	J153329.17+142537.8	2.564	BOSS	59	3898
J153456.02+215342.3	1.6695	SDSS-HW	J153455.85+215324.7	2.529	BOSS	156	1700
J153954.74+314629.3	1.8692	SDSS-HW	J153952.46+314625.2	2.235	BOSS	256	1075
J155325.61+192140.0	2.0096	[OIII]	J155325.89+192137.7	2.098	MagE	44	5576
J155422.88+124438.0	1.8166	SDSS-HW	J155424.39+124431.5	2.394	BOSS	202	1350
J155743.07+043439.2	1.8611	SDSS-HW	J155741.27+043425.3	2.354	BOSS	264	565
J155947.73+494307.3	1.8615	MgII	J155946.28+494326.7	1.945	LRIS	210	1743
J160547.59+511330.2	1.7841	SDSS-HW	J160546.66+511322.6	1.849	LRIS	102	3813
J161930.94+192620.9	1.7819	SDSS-HW	J161929.78+192645.4	2.39	BOSS	258	538
J162738.63+460538.4	3.8141	[OIII]	J162737.25+460609.3	4.11	ESI	253	1959
J163121.74+433317.3	2.0172	SDSS-HW	J163123.57+433317.3	2.631	BOSS	172	4088
J165716.85+310513.0	2.1331	MgII	J165716.52+310524.5	2.395	MODS1	98	5222
J214620.69-075250.6	2.115	[OIII]	J214620.99-075303.8	2.577	MagE	120	4869
J220248.61+123645.5	2.0692	[OIII]	J220248.31+123656.3	2.512	BOSS	100	9466
J225535.67-000156.8	1.7327	SDSS-HW	J225537.62-000144.1	2.412	BOSS	280	352
J225550.44-000917.7	2.0107	SDSS-HW	J225549.55-000927.7	2.129	BOSS	140	1233
J233845.19-000327.2	2.4394	[OIII]	J233845.45-000331.8	2.99	XSHOOTER	51	3745

^a The emission-line analyzed for measuring z_{fg} . SDSS-HW stands for adopting the redshift measured by Hewett & Wild (2010) directly.

The goal of our experiment is to measure the average velocity fields of the absorption from C⁺, C³⁺, and Mg⁺

ions associated with the CGM of the galaxies hosting $z \sim 2$ quasars.

From our QPQ survey⁴, we analyze a subset of systems

⁴ <http://www.qpqsurvey.org>

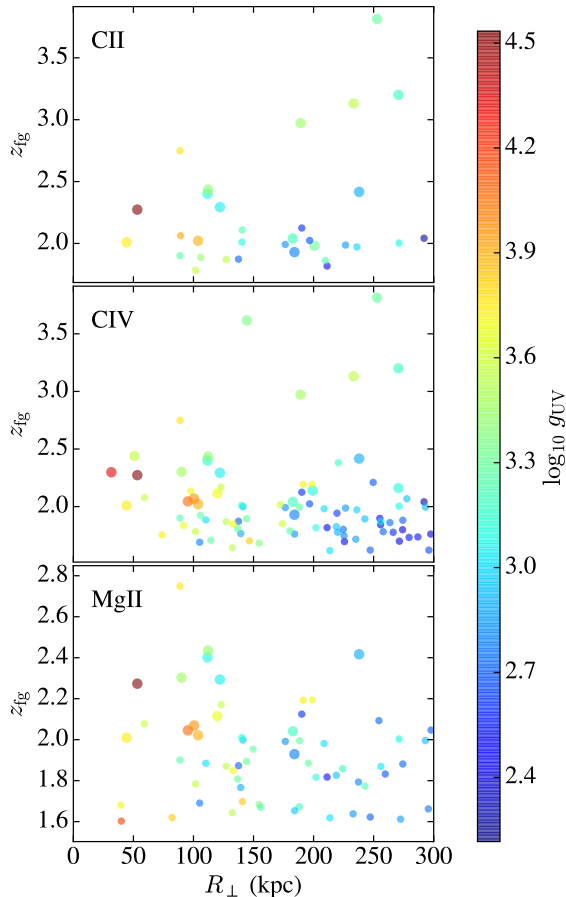


Figure 1. These panels summarize properties of the QPQ9 dataset. The QPQ survey selects quasar pairs of $R_{\perp} < 300$ kpc and $z_{\text{fg}} > 1.6$. Assuming that the foreground quasars emit isotropically and at a distance equal to the impact parameter, the enhancement in the UV flux relative to the extragalactic UV background, g_{UV} , can be estimated. Large symbols correspond to foreground quasars with the most precise redshift measurement from [O III] 5007, while small symbols correspond to z_{fg} measurements from Mg II 2800, H α , or H β emission. The top panel shows quasar pairs with coverage of C II 1334 at z_{fg} in the background quasar spectra. The middle panel shows pairs with coverage of C IV 1548. The bottom panel shows pairs with coverage of Mg II 2796.

that pass within transverse separation $R_{\perp} < 300$ kpc from a foreground quasar with $z_{\text{fg}} > 1.6$. We restrict the sample to foreground quasars with redshift measured from Mg II 2800, [O III] 5007, or H α emission, giving a precision of 300 km s^{-1} or better and an average offset from the systemic redshift of 100 km s^{-1} or less. According to Shen et al. (2016a), the [O III] emission-line redshifts have the smallest scatter (intrinsic scatter and measurement error combined) of 68 km s^{-1} about the systemic redshift, and we analyze the sub-sample with [O III] redshifts separately. The [O III] line has an average blueshift of 48 km s^{-1} about the systemic redshift, which has been added when we compute the redshift of the line. The scatter and average offset of [O III] redshifts reported by Shen et al. (2016a) is consistent with the numbers reported by Boroson (2005) using a larger but lower redshift sample. Systemic redshifts measured from Mg II have a precision of 226 km s^{-1} according to Shen et al. (2016a), and we have taken into account their reported median blueshift of 57 km s^{-1} of Mg II

from the systemic. We note that Richards et al. (2002) reported a median redshift of 97 km s^{-1} of Mg II from [O III] using a larger but lower redshift sample. In QPQ8, we quantified the precision of H α to be 300 km s^{-1} and the median offset from the systemic redshift is close to zero, consistent with the velocity shifts measured by Shen et al. (2011). Although H β is a narrow emission-line, we do not consider its redshift sufficiently reliable for use as systemic redshift. H β redshifts have a large scatter about the systemic $\approx 400 \text{ km s}^{-1}$, and a large average offset about the systemic $\approx 100 \text{ km s}^{-1}$ (Shen et al. 2016a, QPQ8). We further add to the QPQ dataset with quasar pairs selected from the public dataset of igmspec⁵, which includes the spectra from the quasar catalogs based upon the Sloan Digital Sky Survey Seventh Data Release (Schneider et al. 2010) and the Twelfth Data Release (Pâris et al. 2017). We only select pairs with z_{fg} measured by Hewett & Wild (2010) using the Mg II 2800 emission-line, and we add the median blueshift of Mg II from the systemic to these redshifts. We reach a final sample size of 112. Figure 1 summarizes the experimental design. We refer the reader to previous QPQ publications for the details on the redshift centroiding algorithm, data reduction, and continuum normalization (QPQ6; QPQ8).

As in the previous QPQ papers, we select the quasar pairs to have redshift difference $> 3000 \text{ km s}^{-1}$, to exclude physically associated binary quasars. The cut on velocity difference is motivated by the typical redshift uncertainty of $\approx 500 \text{ km s}^{-1}$ of the background quasars. In QPQ8, it was required that the observed wavelengths of the metal ion transitions fall outside the Ly α forest of the background quasar. In this paper, we exclude a small window around the Ly α emission, in addition to the Ly α forest, from analysis. For stacked profile analysis, a good estimate of the continuum level is necessary. In QPQ8 we found that absorption associated to the foreground quasar occurs within $\pm 2000 \text{ km s}^{-1}$ around z_{fg} . Therefore, it is desirable to keep a $\approx \pm 3000 \text{ km s}^{-1}$ window relatively free of contamination from Ly α forest. Taking into account the redshift uncertainties, we decide that at least one transition among C II 1334, C IV 1548, and Mg II 2796 at z_{fg} must lie redward of $(1215.6701 + 20) \times (1 + z_{\text{bg}}) \text{ \AA}$, for a pair to be included in the analysis.

Furthermore, we include only those spectra with average signal-to-noise ratio (S/N) exceeding 5.5 per rest-frame \AA in a $\pm 3000 \text{ km s}^{-1}$ window centered on the observed wavelengths of the metal ion transitions. This criterion is a compromise between maximizing sample size versus maintaining good data quality on the individual sightlines. We find that $\text{S/N} > 5.5$ per rest-frame \AA is necessary for properly estimating the continuum, as well as identifying mini-broad absorption line systems associated to the background quasar, which will significantly depress the flux level. We also require that the region of the spectrum that is $\pm 3000 \text{ km s}^{-1}$ around a considered metal ion transition does not overlap with strong atmospheric O₂ bands. The O₂ A- and B-band span $7595\text{--}7680 \text{ \AA}$ and $6868\text{--}6926 \text{ \AA}$ respectively.

Table 1 lists the full QPQ9 sample. In Table 2, we first

⁵ <https://github.com/specdb/igmspec>

Figure 2. Mean and median absorption centered at C II 1334, C IV 1548, and Mg II 2796 of the foreground quasars for all QPQ9 pairs. The composites are shown in thin, black. Overplotted on the composites are Gaussians, normalized to pseudo-continuum far away from a velocity of 0 km s^{-1} relative to z_{fg} , and are shown in thick, blue. For the doublets, a second Gaussian with a fixed mean separation and a tied standard deviation is included in the modeling. The absorptions frequently exhibit large velocity widths. The dashed lines mark the centroids, which show small positive velocity offsets from z_{fg} . The 1σ modeling error for the centroid and dispersion of the C II mean stack are 28 km s^{-1} and 29 km s^{-1} respectively, which is also the typical modeling errors of the other stacks.

list the sample size, the median z_{fg} , and the median R_{γ} of the quasar pairs that survive the above selection criteria for C II 1334, C IV 1548, and Mg II 2796 respectively. We then provide the summary for the sub-sample with z_{fg} measured from [O III].

3. ANALYSIS

3.1. Stacked Profiles

We create composite spectra that average over the intrinsic scatter in quasar environments, continuum placement errors, and redshift errors. The individual spectra of background quasars are shifted to the rest-frame of the foreground quasars at the transitions of interest. Each spectrum has been linearly interpolated onto a fixed velocity grid centered at z_{fg} with bins of 100 km s^{-1} . For a velocity bin of this size, it is unnecessary to smooth the data to a common spectral resolution. The individual spectra are then combined with a mean or a median

statistic. Bad pixels in the individual spectra have been masked before generating the composites. Since each quasar pair gives an independent probe of the CGM, each pair has an equal weighting in the stacked profiles, i.e. we do not weight the spectra by the measured S/N near the metal ion transitions. Scatter in the stacked spectra is dominated by randomness in the CGM rather than scatter in the flux of individual observations. The mean statistic of the individual spectra yields a good estimate of the average absorption and preserves equivalent width. The median statistic is less sensitive to outliers, however the averaged equivalent width is smaller and the analysis on the velocity field becomes more uncertain. In the following we present stacked spectra using both the mean and the median statistic.

In Figure 2, we present mean and median stacks of C II 1334, C IV 1548, and Mg II 2796 absorption of the QPQ9 sample. We focus on the analysis results of the C II mean stack. C IV and Mg II are doublet transitions and it is more challenging to interpret their kinematics. Two results are evident in Figure 2: (i) the mean C II stack exhibits excess absorption spanning a large velocity width; (ii) the mean absorption is likely skewed toward positive velocities. To model the absorption, we introduce a Gaussian profile while allowing a constant pseudo-continuum level to vary. We perform χ^2 minimization with each channel given equal weight. From the best-fit to the data, we measure the centroid of the C II stack to be $+208 \text{ km s}^{-1}$ and the 1σ dispersion to be 318 km s^{-1} . The centroid suggests an asymmetry that contradicts the standard expectation, while the dispersion suggests extreme kinematics. The median stack, on the other hand, shows weaker absorption, and the Gaussian model has a centroid with smaller offset and comparable dispersion.

We also create mean and median stack for the sub-sample with [O III] redshifts and model the absorption with Gaussian best-fit. The C II mean stack for this sub-sample has a centroid at $+249 \text{ km s}^{-1}$, and a dispersion of 362 km s^{-1} , consistent with the full sample.

To model the mean and median absorption of C IV 1548 and Mg II 1796, we introduce a second Gaussian with separation equal to the doublet separation (498 km s^{-1} and 769 km s^{-1} respectively), and tie the dispersion of the two lines in a doublet. The modeling results show that the velocity fields of C IV and Mg II are consistent with C II, i.e. large dispersion and centroid is skewed toward positive velocities.

The above analyses are summarized in Table 2. The Gaussian models normalized to pseudo-continuum are overplotted on the data stacks in Figure 2.

Table 2
Summary of the Data and Analysis

Measure	C II 1334	C IV 1548	Mg II 2796
For the Full QPQ9 Sample			
Number of pairs	32	89	65
Median z_{fg}	2.02	1.93	1.89
Median R_{γ}	180	189	155
Centroid of mean stack (km s^{-1})	+208 77	+86 113	+184 127

Table 2 — *Continued*

Measure	C II 1334	C IV 1548	Mg II 2796
1σ dispersion of mean stack (km s^{-1})	318 ± 85	320 ± 100	300 ± 105
Centroid of median stack (km s^{-1})	$+15 \pm 140$	$+251 \pm 124$	-42 ± 301
1σ dispersion of median stack (km s^{-1})	215 ± 200	193 ± 147	270 ± 194
For the Sub-sample with [OIII] Redshifts			
Number of pairs	14	22	15
Median z_{fg}	2.35	2.3	2.27
Median R_{\perp}	183	121	112
Centroid of mean stack (km s^{-1})	$+249 \pm 139$	$+178 \pm 79$	$+263 \pm 122$
1σ dispersion of mean stack (km s^{-1})	362 ± 168	256 ± 53	224 ± 146
Centroid of median stack (km s^{-1})	$+79 \pm 195$	$+112 \pm 126$	$+196 \pm 163$
1σ dispersion of median stack (km s^{-1})	354 ± 433	84 ± 100	229 ± 163

3.2. Interpretation of the asymmetric absorption

Given the small sample size, one must scrutinize the statistical significance of the measured velocity offsets. To assess the statistical significance, we perform a bootstrap analysis by randomly resampling from the full sample 10000 times. We introduce a Gaussian absorption profile to model each bootstrap realization, and quote the standard deviation in the the bootstrap realizations to be the scatter in the centroids of the data. The scatters $\approx 100 \text{ km s}^{-1}$ are comparable to the measured offsets, indicating large intrinsic variation in quasar CGM environments (see also QPQ8). In Figure 3, we show the distribution of the absorption centroids from bootstrapping on the C II mean stack. We find that 98% of the centroids are at positive velocities. We place a generous 3σ upper limit to the small offset of the centroid from z_{fg} for the C II mean absorption at $\delta v < +451 \text{ km s}^{-1}$. Given the large intrinsic scatter, we do not attempt to explore whether there exists relative asymmetry among the C II, C IV, and Mg II absorption.

One may also ask whether the measured positive offsets come from systematic bias in redshift measurements due to the Baldwin effect (Baldwin 1977). Shen et al. (2016b) reported that, the [O III] emission of $z \sim 2$ quasars is more asymmetric and weaker than that in typically less luminous low- z quasars. To test for this potential source of bias, we create another mean stack at C II 1334 by replacing the [O III] redshifts by a Mg II or $\text{H}\alpha$ redshift when available. We are able to replace for 8 out of the 14 systems with [O III] redshifts in the original sample. The new stack is similar in velocity structure and again shows a positive offset $\approx +240 \text{ km s}^{-1}$. We thus conclude that our algorithm for measuring redshifts is not severely biased by the blue wing of the [O III] emission-line.

Motivated by the study of Mg II absorbers surrounding $z \sim 1$ quasars by Johnson et al. (2015), we also generate a mean-stacked spectrum for Mg II 2796 for lower redshift quasar pairs. We select quasars with $0.4 < z_{\text{fg}} < 1.6$ and use the same other selection criteria as the main QPQ9 sample. The quasar pairs are selected from the igmspec database, with z_{fg} measured by Hewett & Wild (2010). For quasars with $z_{\text{fg}} < 0.84$, as redshift determination is dominated by [O III] emission, a shift of $+48 \text{ km s}^{-1}$ is applied to bring the emission-line redshift to the systemic. For quasars with $0.84 < z_{\text{fg}} < 1.6$, as redshift

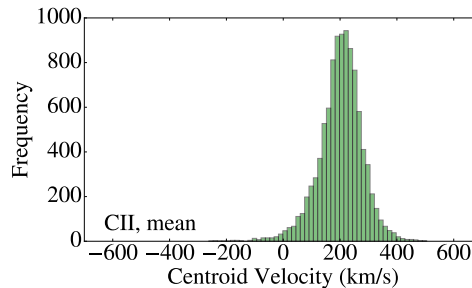


Figure 3. Histogram of the absorption centroids of 10000 bootstrap realizations of the data sample for the C II mean stack. 98% of the centroids are positively offset from z_{fg} .

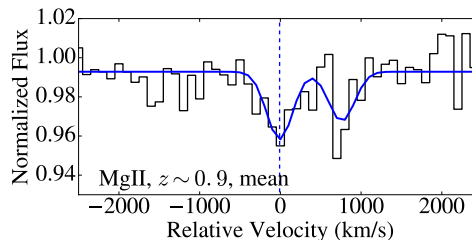


Figure 4. Mean stack at Mg II 2796, for a lower redshift sample of quasar pairs at $z \sim 0.9$. Line-style coding is the same as in Figure 2. The centroid is approximately at 0 km s^{-1} , and the absorption is weaker than the main QPQ9 sample.

determination is dominated by Mg II emission, a shift of 57 km s^{-1} is applied. There are 231 pairs selected, with a median z_{fg} of 0.90 and a median R_{\perp} of 208 kpc. We present the mean stack in Figure 4. The absorption is weaker than the $z \sim 2$ main QPQ9 sample. Gaussian absorption models fitted to the stack recover a centroid of $-9 \pm 388 \text{ km s}^{-1}$ and a dispersion of 161 km s^{-1} . The average offset from 0 km s^{-1} is much smaller than the offsets in the $z \sim 2$ sample.

Since the large scatter in the centroids represents intrinsic variation rather than redshift errors, and the Mg II stack for lower redshift suggests a different centroid, we consider that the asymmetry signal in the $z \sim 2$ sample is likely to be real. In the Discussion section, we discuss two possible explanations for the asymmetry.

3.3. Interpretation of the large velocity fields

Under the assumption that the intrinsic dispersion and the redshift uncertainty add in quadrature to give the observed width, we solve for the intrinsic dispersion in the C II mean stack. For the full QPQ9 sample, with

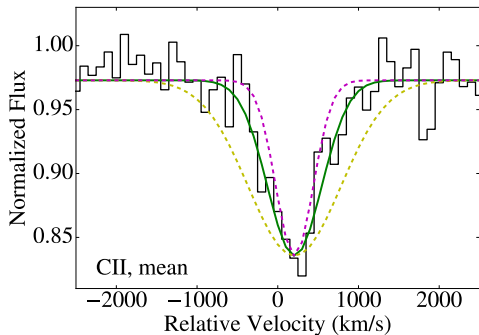


Figure 5. The same C II mean stack shown in the first panel of Figure 2 is shown in thin, black. In thick, green, we overplot the Gaussian absorption model of the Monte Carlo simulations generated from a purely clustering argument. The model from clustering analysis is multiplied to the pseudo-continuum level of the stack of the observational data, shifted to the centroid of the stack of the data, and broadened by the mean redshift error in the data. The model is a good description of the data, with a dispersion within modeling error of the dispersion in the data. We overplot in dashed, yellow an absorption profile with $\sigma_v = 573 \text{ km s}^{-1}$, which is larger than the observed width by three times the standard deviation in the bootstrap analysis. Motions that produce a velocity width larger than this can be ruled out. We overplot in dashed, magenta an absorption profile with $\sigma_v = 231 \text{ km s}^{-1}$, which is smaller than the observed width by three times the modeling error. Unless gravitational and Hubble flows together with redshift error broadening produce a velocity width smaller than this, extra dynamical processes (e.g. outflows) will not be required to explain the observation.

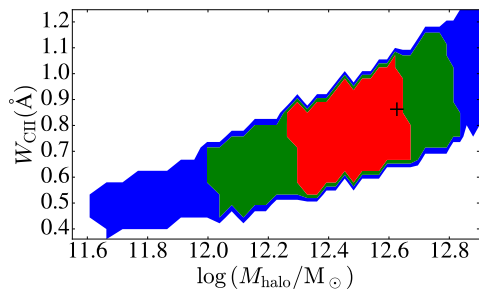


Figure 6. Probability distributions of the parameters W_{CII} and M_{halo} . The plot shows the degeneracy between W_{CII} and M_{halo} in recovering the intrinsic width of the absorption profile. We mark contours for points that produce an absorption profile of width that is 1, 2, 3, and 4 times the modeling error away from the observed intrinsic width. The intrinsic velocity width corresponding to typical QPQ halo mass is marked with a plus sign, and is well contained within the 2σ contour.

the mean $\sigma_{\text{error}(z)}^{\text{full}} = 182 \text{ km s}^{-1}$, we recover $\sigma_{\text{intrinsic}}^{\text{full}} = 261 \text{ km s}^{-1}$. For the sub-sample with [O III] redshifts, we recover $\sigma_{\text{intrinsic}}^{[\text{OIII}]} = 356 \text{ km s}^{-1}$.

Eftekharzadeh et al. (2015) measured the clustering of quasars in the range $2.2 < z < 2.8$ while Rodríguez-Torres et al. (2017) measured the clustering of quasars in the range $1.8 < z < 2.2$. They estimated that these quasars are hosted by dark matter halos with mass $M_{\text{halo}} = 10^{12.5} M_{\odot}$ and $M_{\text{halo}} 10^{12.6} M_{\odot}$ respectively. If dark matter halos hosting QPQ9 quasars have a characteristic mass $10^{12.6} M_{\odot}$ and follow an NFW profile (Navarro et al. 1997) with concentration parameter $c = 4$, at $z \approx 2$ the maximum circular velocity is 345 km s^{-1} . Tormen et al. (1997) found that the maximum circular velocity is ≈ 1.4 times the maximum of the one-dimensional velocity dispersion $\sigma_{1\text{D}}$. Hence, the line-of-sight velocity dispersion typical of QPQ9 halos is

$\sigma_{1\text{D}} = 246 \text{ km s}^{-1}$. We can investigate whether gravitational motions and Hubble flows are sufficient to reproduce the dispersion in the data, using Monte Carlo methods to simulate the absorption signals.

Since C II systems arise in optically thick absorbers, we may adopt the clustering analysis results of QPQ6. In the absence of clustering, the expected number of absorbers per unit redshift interval for Lyman limit systems, super Lyman limit systems, and damped Ly α systems are respectively $\ell_{\text{IGM}}^{\text{LLS}}(z) \approx 1.05((1+z)/(1+2.5))^{2.1}$, $\ell_{\text{IGM}}^{\text{SLLS}}(z) \approx 0.44((1+z)/(1+2.5))^{2.1}$, and $\ell_{\text{IGM}}^{\text{DLA}}(z) \approx 0.2((1+z)/(1+2.5))^{2.1}$. The quasar-absorber correlation functions for Lyman limit systems, super Lyman limit systems, and damped Ly α systems are respectively $\xi_{\text{QA}}^{\text{LLS}}(r) = (r/(12.5 h^{-1} \text{ Mpc}))^{-1.68}$, $\xi_{\text{QA}}^{\text{SLLS}}(r) = (r/(14.0 h^{-1} \text{ Mpc}))^{-1.68}$, and $\xi_{\text{QA}}^{\text{DLA}}(r) = (r/(3.9 h^{-1} \text{ Mpc}))^{-1.6}$. For each quasar pair, we calculate the expected number of optically thick absorbers within $\pm 3000 \text{ km s}^{-1}$ at a distance R_{\perp} from the foreground quasar and at z_{fg} . Then we generate 1000 mock sightlines. The number of absorbers for each mock spectrum is randomly selected from a Poisson distribution with mean equal to the expected number calculated as above. The absorbers are randomly assigned Hubble velocities, with a probability distribution according to the quasar-absorber correlation functions. The absorbers are randomly assigned additional peculiar velocities drawn from a normal distribution with mean equal to 0 km s^{-1} and scatter equal to $\sigma_{1\text{D}}$. For each absorber, we assume a rest equivalent width for C II W_{CII} and a Gaussian absorption profile. We repeat the above procedure for all 32 quasar pairs, and create a mean stack of the 32000 mock spectra generated. We fit a Gaussian absorption profile multiplied to a constant continuum level to model the stack of mock spectra. We adjust the W_{CII} adopted for the absorbers until the amplitude of the best-fit Gaussian of the stack of mock spectra matches the amplitude of the stack of the observational data. We find that $W_{\text{CII}} = 0.8 \text{ \AA}$ well reproduces the amplitude, and the dispersion of the Gaussian absorption model is insensitive to the assumed W_{CII} or line profile for one absorber.

In Figure 5, we show a comparison of the observational data stack and the Gaussian absorption model of the Monte Carlo simulations. In the figure, the Gaussian absorption model is broadened by the mean redshift error in the model. The resulting stack of mock spectra has a 1σ dispersion of 284 km s^{-1} . This is about 1σ modeling error away from the intrinsic dispersion in the C II mean stack for the full sample, and about 3 times the modeling error away from the intrinsic dispersion in the stack of the sub-sample with [O III] redshifts. We also test for the sensitivity of this measured dispersion to the correlation functions adopted. The QPQ6 clustering analysis is performed on only the strongest absorber near z_{fg} , and a low R_{\perp} sightline may in fact intercept more than one optically thick absorber. We double the number of absorbers for each mock sightline, and find the measured dispersion only increases by several km s^{-1} . Thus, the hypothesis that the observed velocity width is only produced by a combination of gravitational motions and Hubble flows cannot be ruled out. Extra dynamical processes are not necessary to explain the large velocity fields.

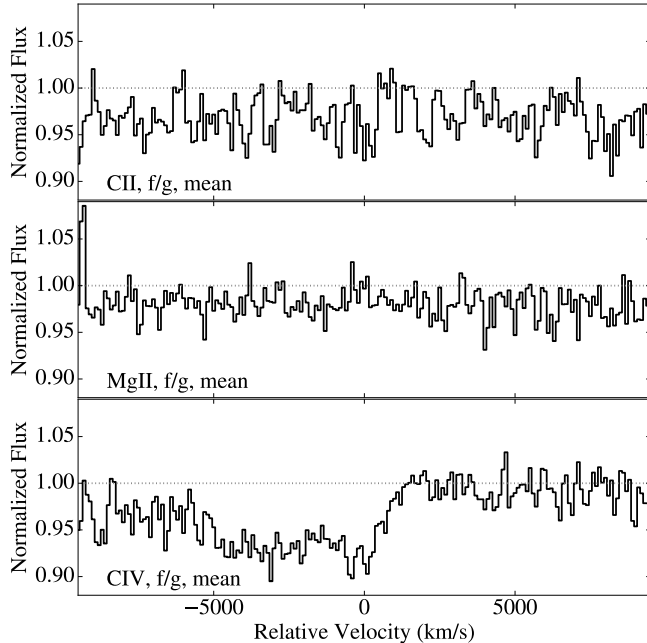


Figure 7. Mean stacks of the foreground quasar spectra at C II 1334, C IV 1548, and Mg II 2796 for the QPQ9 sample. For C II and Mg II, the mean absorption is weaker than that in the background stacks, and there is no evidence for an excess at z_{fg} . The stack for C IV, which includes line-of-sight absorbers at all distances, shows a large, blueshifted mean velocity field.

From the bootstrap analysis of the observed dispersion, a width of $\sigma_v > 573 \text{ km s}^{-1}$ would be larger than the observed by three times the scatter (overplotted in Figure 5). In other words, taking into account the redshift errors, motions in addition to gravitational and Hubble flows that will produce an intrinsic dispersion $\sigma_v > 543 \text{ km s}^{-1}$ can be ruled out.

On the contrary, $\sigma_{\text{1D}} < 114 \text{ km s}^{-1}$ together with Hubble velocities and broadening by redshift errors will result in a velocity width that is more than three times the modeling error away from the observed width (overplotted in Figure 5). This implies that, unless the characteristic $M_{\text{halo}} < 10^{11.6} M_{\odot}$, additional dynamical processes are not required to explain the observed width.

In Figure 6, We show the probability distributions of the degenerate parameters W_{CII} and M_{halo} in recovering the intrinsic width of the absorption profile. We require that the amplitude of the absorption is reproduced within 3 times its modeling error, and mark contours for points in $(W_{\text{CII}}, M_{\text{halo}})$ -space that produce an absorption profile of width within 1, 2, 3, and 4 times the modeling error of the observed intrinsic width. From the figure, a higher W_{CII} means the M_{halo} that will reproduce the observed width is higher. If there are no extra dynamical processes, the intrinsic velocity width corresponding to typical QPQ halo mass is well contained within the 2σ contour.

3.4. Line-of-sight absorption

In the previous QPQ papers, we argued that optically thick absorbers in the vicinity of quasars are distributed anisotropically. We now have the means to show this anisotropic clustering explicitly. Given that the techniques for stacking spectra are established, it is straightforward to apply the same techniques to stack the fore-

ground quasar spectra. In Figure 7, we present mean stacks of foreground quasar spectra for the QPQ9 sample. We require that the spectra survive a S/N cut of 5.5 per rest-frame \AA at C II 1334, C IV 1548, or Mg II 2796 at z_{fg} . In contrast to the large equivalent widths exhibited in the stacks of background spectra, C II and Mg II mean absorption along the line-of-sight to the foreground quasars is weaker, and an excess at z_{fg} is absent. This supports a scenario where the ionizing radiation of the foreground quasars are anisotropic and/or intermittent. For C IV 1548, this stack of all line-of-sight absorbers, which include absorbers intrinsic to and far away from the quasar, shows a large, blueshifted velocity field. This excess C IV absorption has been well studied as narrow associated absorption line systems (e.g., Wild et al. 2008).

4. DISCUSSION

In the following, we explore two possible explanations for the putative non-dynamical process that provides the asymmetry.

One possibility is an asymmetric radiation field that preferentially ionizes the gas moving toward the observer, where the quasar is known to shine. Alternatively, the asymmetric radiation field may preferentially ionizes the gas at smaller Hubble velocity than the quasar. In Figure 8, we show a cartoon of a quasar that is blocked in the direction pointing away from the observer. The gas observed in absorption preferentially lies behind the quasar. The asymmetric absorption arises from a transverse proximity effect. Roos et al. (2015) and Gabor & Bournaud (2014) performed simulations of a high-redshift galaxy including thermal AGN feedback and calculated radiative transfer in post-processing. They found the ionization radiation is typically asymmetric, due to either a dense clump that lies on one edge of the black hole or the black hole’s location being slightly above the disk.

Another possible explanation arises from the finite lifetime of quasar episodes. Figure 9 presents a cartoon for a light travel time argument. Light from the background quasar will travel smaller distance to reach the gas behind the foreground quasar than the gas in front of it. The light from the background quasar may arrive at the gas behind the foreground quasar before the ionizing radiation from the foreground quasar arrives. In QPQ7 and QPQ8, we reported that the enhancement in metal ion absorption relative to IGM average extends to at least $\approx 200 \text{ kpc}$. This distance corresponds to a light travelling time of $\sim 10^6 \text{ Myr}$, which lies within existing constraints of quasar lifetime from observations (e.g. Martini 2004) and simulations (e.g. Hopkins et al. 2005).

As a test of reasonableness, we calculate that, at $R_{\perp} \approx 50\text{--}150 \text{ kpc}$, radial speeds relative to the foreground quasar of $500\text{--}700 \text{ km s}^{-1}$ and quasar opening angles of $120^{\circ}\text{--}140^{\circ}$ may reproduce the observed centroid and intrinsic dispersion of the C II mean absorption. The first explanation above to asymmetric absorption requires that the quasars emit their ionizing radiation anisotropically, while the second explanation requires the quasars emit their ionizing radiation intermittently. Both explanations will require the line-of-sight motions of the gas to be in either outflow or Hubble flow. Were the gas flowing into the galaxy instead, the velocity

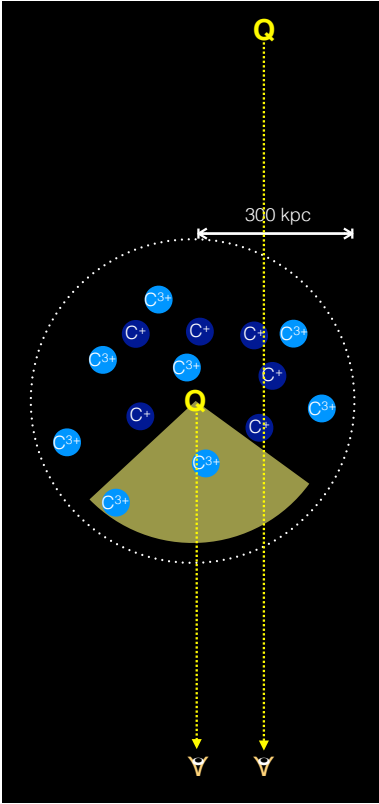


Figure 8. A cartoon showing a unipolar quasar. The gas observed in low- to intermediate-ion absorption preferentially lies behind the quasar, and is shadowed from the ionizing radiation.

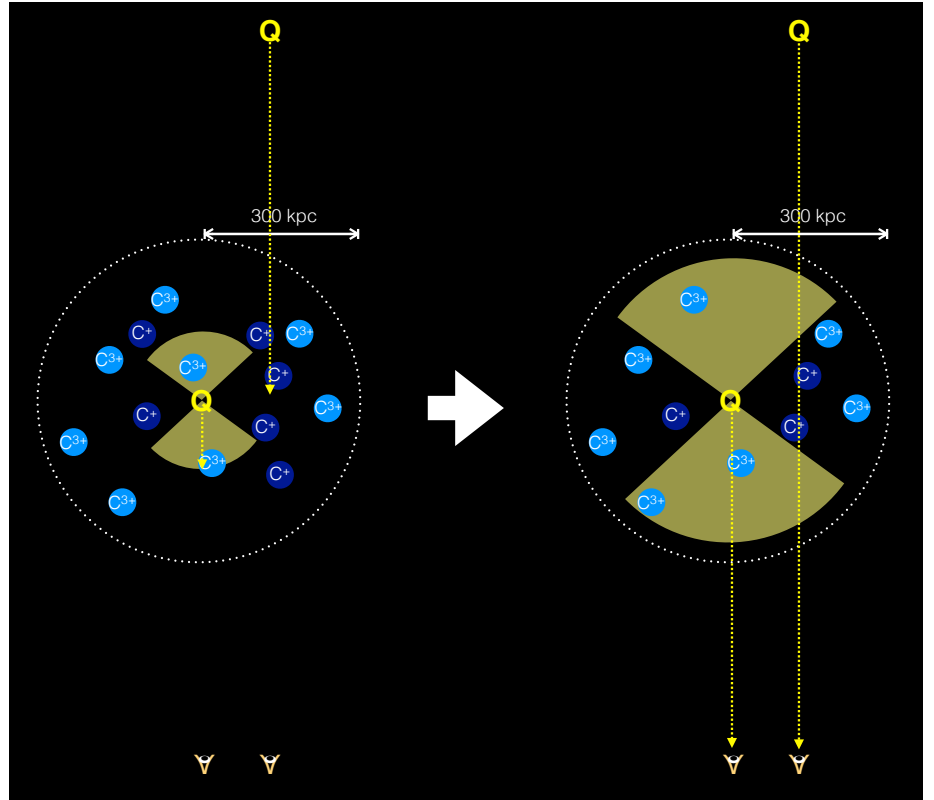


Figure 9. A cartoon showing the finite lifetime of quasar episodes as an explanation to the asymmetric absorption. The setup on the left shows that the foreground quasar has not been shining long enough for its ionizing radiation to reach the gas behind it, when the light from the background quasar reaches. The setup on the right shows the scenario after an amount of time comparable to the light travelling time across CGM scale. Gas in front of the foreground quasar has been ionized, by the time the light from the background quasar reaches.

centroid would be negative.

Motivated by the asymmetry found in metal ion absorption in the CGM using precise z_{fg} measurements, and the asymmetry found by Kirkman & Tytler (2008) in H I on larger scales, we are assembling a sample of quasar pairs with precise z_{fg} measurements to study this asymmetry in H I (J. F. Hennawi et al. 2017, in preparation). In conclusion, we observe large and positively skewed velocity fields in absorption, of metal ions in the CGM of $z \sim 2$ massive galaxies hosting quasars. We argue that the velocity fields can be explained if the detected gas is in gravitational motion, Hubble flow, or outflow, and the quasars either shine preferentially toward the observer or shine intermittently.

JXP and MWL acknowledge support from the National Science Foundation (NSF) grants AST-1010004 and AST-1412981. The authors gratefully acknowledge the support which enabled these observations at the Keck, Gemini, Large Binocular Telescope, Very Large Telescope, Las Campanas, and Palomar Observatories. MWL thanks T.-K. Chan for a discussion on CGM simulations and Chi Po Choi for a discussion on statistics.

REFERENCES

- Baldwin, J. A. 1977, *ApJ*, 214, 679
 Bergeron, J., & Boisse, P. 1991, *Advances in Space Research*, 11, 241
 Boroson, T. 2005, *AJ*, 130, 381
 Cantalupo, S., Arrigoni-Battaia, F., Prochaska, J. X., Hennawi, J. F., & Madau, P. 2014, *Nature*, 506, 63
 Churchill, C. W., Kacprzak, G. G., Steidel, C. C., Spitler, L. R., Holtzman, J., Nielsen, N. M., & Trujillo-Gomez, S. 2012, *ApJ*, 760, 68
 Eftekharzadeh, S., Myers, A. D., White, M., Weinberg, D. H., Schneider, D. P., Shen, Y., Font-Ribera, A., Ross, N. P., Paris, I., & Streblyanska, A. 2015, *MNRAS*, 453, 2779
 Fumagalli, M., Prochaska, J. X., Kasen, D., Dekel, A., Ceverino, D., & Primack, J. R. 2011, *MNRAS*, 418, 1796
 Gabor, J. M., & Bournaud, F. 2014, *MNRAS*, 441, 1615
 Gauthier, J.-R. 2013, *MNRAS*, 432, 1444
 Hennawi, J. F., Prochaska, J. X., Burles, S., Strauss, M. A., Richards, G. T., Schlegel, D. J., Fan, X., Schneider, D. P., Zakamska, N. L., Oguri, M., Gunn, J. E., Lupton, R. H., & Brinkmann, J. 2006, *ApJ*, 651, 61
 Hennawi, J. F., Prochaska, J. X., Cantalupo, S., & Arrigoni-Battaia, F. 2015, *Science*, 348, 779
 Hewett, P. C., & Wild, V. 2010, *MNRAS*, 405, 2302
 Hopkins, P. F., Hernquist, L., Martini, P., Cox, T. J., Robertson, B., Di Matteo, T., & Springel, V. 2005, *ApJ*, 625, L71
 Johnson, S. D., Chen, H.-W., & Mulchaey, J. S. 2015, *MNRAS*, 452, 2553
 Kereš, D., Katz, N., Fardal, M., Davé, R., & Weinberg, D. H. 2009, *MNRAS*, 395, 160
 Kirkman, D., & Tytler, D. 2008, *MNRAS*, 391, 1457
 Lau, M. W., Prochaska, J. X., & Hennawi, J. F. 2016, *ApJS*, 226, 25
 Martin, C. L. 2005, *ApJ*, 621, 227
 Martini, P. 2004, *Coevolution of Black Holes and Galaxies*, 169
 Muzahid, S., Kacprzak, G. G., Churchill, C. W., Charlton, J. C., Nielsen, N. M., Mathes, N. L., & Trujillo-Gomez, S. 2015, *ApJ*, 811, 132
 Navarro, J. F., Frenk, C. S., & White, S. D. M. 1997, *ApJ*, 490, 493

- Páris, I., Petitjean, P., Ross, N. P., Myers, A. D., Aubourg, É., Streblyanska, A., Bailey, S., Armengaud, É., Palanque-Delabrouille, N., Yèche, C., Hamann, F., Strauss, M. A., Albareti, F. D., Bovy, J., Bizyaev, D., Niel Brandt, W., Brusa, M., Buchner, J., Comparat, J., Croft, R. A. C., Dwelly, T., Fan, X., Font-Ribera, A., Ge, J., Georgakakis, A., Hall, P. B., Jiang, L., Kinemuchi, K., Malanushenko, E., Malanushenko, V., McMahon, R. G., Menzel, M.-L., Merloni, A., Nandra, K., Noterdaeme, P., Oravetz, D., Pan, K., Pieri, M. M., Prada, F., Salvato, M., Schlegel, D. J., Schneider, D. P., Simmons, A., Viel, M., Weinberg, D. H., & Zhu, L. 2017, *A&A*, 597, A79
- Prochaska, J. X., Hennawi, J. F., Lee, K.-G., Cantalupo, S., Bovy, J., Djorgovski, S. G., Ellison, S. L., Lau, M. W., Martin, C. L., Myers, A., Rubin, K. H. R., & Simcoe, R. A. 2013a, *ApJ*, 776, 136
- Prochaska, J. X., Hennawi, J. F., & Simcoe, R. A. 2013b, *ApJ*, 762, L19
- Prochaska, J. X., Lau, M. W., & Hennawi, J. F. 2014, *ApJ*, 796, 140
- Prochaska, J. X., Weiner, B., Chen, H.-W., Mulchaey, J., & Cooksey, K. 2011, *ApJ*, 740, 91
- Rakic, O., Schaye, J., Steidel, C. C., & Rudie, G. C. 2012, *ApJ*, 751, 94
- Richards, G. T., Vanden Berk, D. E., Reichard, T. A., Hall, P. B., Schneider, D. P., SubbaRao, M., Thakar, A. R., & York, D. G. 2002, *AJ*, 124, 1
- Rodríguez-Torres, S. A., Comparat, J., Prada, F., Yepes, G., Burtin, E., Zarrouk, P., Laurent, P., Hahn, C., Behroozi, P., Klypin, A., Ross, A., Tojeiro, R., & Zhao, G.-B. 2017, *MNRAS*, 468, 728
- Roos, O., Juneau, S., Bournaud, F., & Gabor, J. M. 2015, *ApJ*, 800, 19
- Rubin, K. H. R., Prochaska, J. X., Koo, D. C., Phillips, A. C., Martin, C. L., & Winstrom, L. O. 2014, *ApJ*, 794, 156
- Rupke, D. S., Veilleux, S., & Sanders, D. B. 2005, *ApJS*, 160, 115
- Schneider, D. P., Richards, G. T., Hall, P. B., Strauss, M. A., Anderson, S. F., Boroson, T. A., Ross, N. P., Shen, Y., Brandt, W. N., Fan, X., Inada, N., Jester, S., Knapp, G. R., Krawczyk, C. M., Thakar, A. R., Vanden Berk, D. E., Voges, W., Yanny, B., York, D. G., Bahcall, N. A., Bizyaev, D., Blanton, M. R., Brewington, H., Brinkmann, J., Eisenstein, D., Frieman, J. A., Fukugita, M., Gray, J., Gunn, J. E., Hibon, P., Ivezić, Ž., Kent, S. M., Kron, R. G., Lee, M. G., Lupton, R. H., Malanushenko, E., Malanushenko, V., Oravetz, D., Pan, K., Pier, J. R., Price, III, T. N., Saxe, D. H., Schlegel, D. J., Simmons, A., Snedden, S. A., SubbaRao, M. U., Szalay, A. S., & Weinberg, D. H. 2010, *AJ*, 139, 2360
- Shen, Y., Brandt, W. N., Richards, G. T., Denney, K. D., Greene, J. E., Grier, C. J., Ho, L. C., Peterson, B. M., Petitjean, P., Schneider, D. P., Tao, C., & Trump, J. R. 2016a, *ApJ*, 831, 7
- Shen, Y., Horne, K., Grier, C. J., Peterson, B. M., Denney, K. D., Trump, J. R., Sun, M., Brandt, W. N., Kochanek, C. S., Dawson, K. S., Green, P. J., Greene, J. E., Hall, P. B., Ho, L. C., Jiang, D., Kinemuchi, K., McGreer, I. D., Petitjean, P., Richards, G. T., Schneider, D. P., Strauss, M. A., Tao, C., Wood-Vasey, W. M., Zu, Y., Pan, K., Bizyaev, D., Ge, J., Oravetz, D., & Simmons, A. 2016b, *ApJ*, 818, 30
- Shen, Y., Richards, G. T., Strauss, M. A., Hall, P. B., Schneider, D. P., Snedden, S., Bizyaev, D., Brewington, H., Malanushenko, V., Malanushenko, E., Oravetz, D., Pan, K., & Simmons, A. 2011, *ApJS*, 194, 45
- Somerville, R. S., & Davé, R. 2015, *ARA&A*, 53, 51
- Steidel, C. C., Erb, D. K., Shapley, A. E., Pettini, M., Reddy, N., Bogosavljević, M., Rudie, G. C., & Rakic, O. 2010, *ApJ*, 717, 289
- Tormen, G., Bouchet, F. R., & White, S. D. M. 1997, *MNRAS*, 286, 865
- Tripp, T. M., Meiring, J. D., Prochaska, J. X., Willmer, C. N. A., Howk, J. C., Werk, J. K., Jenkins, E. B., Bowen, D. V., Lehner, N., Sembach, K. R., Thom, C., & Tumlinson, J. 2011, *Science*, 334, 952
- Tumlinson, J., Thom, C., Werk, J. K., Prochaska, J. X., Tripp, T. M., Katz, N., Davé, R., Oppenheimer, B. D., Meiring, J. D., Ford, A. B., O'Meara, J. M., Peebles, M. S., Sembach, K. R., & Weinberg, D. H. 2013, *ApJ*, 777, 59
- Weiner, B. J., Coil, A. L., Prochaska, J. X., Newman, J. A., Cooper, M. C., Bundy, K., Conselice, C. J., Dutton, A. A., Faber, S. M., Koo, D. C., Lotz, J. M., Rieke, G. H., & Rubin, K. H. R. 2009, *ApJ*, 692, 187
- Wild, V., Kauffmann, G., White, S., York, D., Lehnert, M., Heckman, T., Hall, P. B., Khare, P., Lundgren, B., Schneider, D. P., & vanden Berk, D. 2008, *MNRAS*, 388, 227
- Zahedy, F. S., Chen, H.-W., Rauch, M., Wilson, M. L., & Zabludoff, A. 2016, *MNRAS*, 458, 2423